Nano Research
2020, 13(1): 95–104

ISSN 1998-0124 CN 11-5974/O4
https://doi.org/10.1007/s12274-019-2578-2

Research Article

Transformation between nanosheets and nanowires structure in MnO_2 upon providing Co^{2+} ions and applications for microwave absorption

Lulu Song, Yuping Duan (✉), Jia Liu, and Huifang Pang (✉)

Key Laboratory of Solidification Control and Digital Preparation Technology (Liaoning Province), School of Materials Science and Engineering, Dalian University of Technology, Dalian 116085, China

Received: 8 October 2019 / **Revised:** 20 November 2019 / **Accepted:** 22 November 2019

ABSTRACT

The phase transition process of the MnO_2 phase with increases in Co^{2+} doping can be described by the Ouroboros symbol. The undoped sample is pure δ-MnO_2 with nanosheets structures. Then a small amount of Co^{2+} ions changes the final products and generates α-MnO_2 nanofibres in the δ-MnO_2 matrix. The products become pure α-MnO_2 with an appropriate amount of Co added. However, when the Co amount continues to increase, the amount of α-MnO_2 decreases in the products and turns back to form pure δ-MnO_2 in the end. Analysing the electromagnetic absorption performance, the relationship between the properties and the proportion of δ-MnO_2/α-MnO_2 in the powders adjusted by Co^{2+} doping has been explored, and the composites of δ-/α-MnO_2 show better absorption ability than the single-phase samples. As a result, the optimal reflection loss (RL) is –54.8 dB, and the effective absorption bandwidth can cover the Ku band at a thickness of 2.2 mm and the X band at a thickness of 3.1 mm with 50 wt.% filler loading ratios. This research might shed new light on the improvement of novel microwave absorption materials.

KEYWORDS

phase transitions, self-assembly, impedance matching, microwave absorption

1 Introduction

Due to the advantages of having a low cost and being nontoxic, along with flexible crystalline phases and morphologies and great physical and chemical properties, manganese dioxide (MnO_2) has been studied for energy storage systems, catalysis, sorption treatment and microwave absorption [1–4]. There are some studies on the relationship between the morphologies of MnO_2 and absorption performance. MnO_2 nanofibres with smaller diameters have preferable absorption capability, and special structures, such as hollow microspheres and hollow urchinlike nanostructures, can improve the microwave absorption properties to some degree [5–7]. However, there are few studies on how the phase structure of MnO_2 affects its wave absorption performance. It is very important to clarify the structure-activity relationship between the phase structure and its wave absorbing performance for the design of material structure and optimization of wave absorbing performance.

Doping has proven to be an effective strategy to improve the absorbing performance through permanent dipolar polarization and doping magnetic ions, which can enhance the magnetic properties of samples [8–12]. Cobalt (Co), a kind of magnetic transitional metal element, is usually studied as a doping atom for metal oxides, such as NiO, Fe_3O_4, Fe_2O_3, ZnO, and Mn_3O_4, and Co doping can influence the structural, magnetic and optical properties of the samples [13–19]. It has been confirmed that the introduction of Co can broaden the microwave absorption bandwidths of cryptomelane (α-MnO_2), and its maximum reflection loss (RL) can reach −40 dB, with a thickness of 2.5 mm [20]. Co-doped Mn_3O_4 reached a maximum RL of −24.0 dB at 4.8 GHz with a thickness of 4 mm [21]. In our previous research, Co doping effectively enhanced the absorption performance of α-MnO_2 [22]. However, these studies focused on the influence of lattice distortion after doping but did not refer to phase transition. From many reports, δ-MnO_2 is not a stable phase. Ya Chen et al. [23] discovered spiny-fibre morphology in Co-doped MnO_2. Liu et al. [24] studied MnO_2 as a catalyst which induced partly transformation of δ-MnO_2 to α-MnO_2 in the reaction. The phase transition is a complex process, and the relationship between phase transition and performance is a deserving field of research [25, 26].

In this paper, accurate regulation of MnO_2 phase crystallinity was realized by controlling Co content. The mechanism of phase crystallinity has been systematically studied, and the absorption performance of Co-doped MnO_2 with varying phases is investigated for 2–18 GHz. This study makes up for the gap in cation-caused phase transitions of MnO_2.

2 Experimental section

2.1 Synthesis of Co-doped MnO_2

All samples were synthesized by the hydrothermal method. The synthesis procedure can be described as follows. First, $KMnO_4$ (36 mmol) was added to 100 mL distilled water with stirring until it dissolved completely. Then, the $MnSO_4{\cdot}H_2O$

Address correspondence to Yuping Duan, duanyp@dlut.edu.cn; Huifang Pang, huifangpang@dlut.edu.cn

(6 mmol) and $CoSO_4·7H_2O$ (x mmol) were added into distilled water (25 mL). Then, the $KMnO_4$ solution was dropped into the mixed solution over a period of 30 min under continuous magnetic stirring. The homogeneous solution was transferred into a Teflon-lined stainless-steel autoclave and reacted at 180 °C for 24 h. Then, the obtained product was rinsed with distilled water several times to remove the undesired soluble ions, and the precipitate was dried at 110 °C for 24 h. The samples were marked as Cx, where x represented the Co millimolar weight.

2.2 Characterization

The crystal structures of the as-made powders were determined by X-ray powder diffraction (XRD, EMPYREAN) analysis with Cu Kα radiation. The morphology, shape and size of the samples were tested with field emission scanning electron microscopy (SEM, SUPRA55) and transmission electron microscopy (TEM, TECNAI). The surface oxide states of the samples were measured by X-ray photoelectron spectroscopy (XPS, Thermo ESCALAB 250XI). The existence of elements in the samples was confirmed by X-ray fluorescence spectrometry (XRF, SHIMADZU). The relative complex permittivity versus frequency was determined by coaxial refection/transmission using an Aglient 8722ES vector network analyser in the frequency range of 2–18 GHz. A sample containing 50 wt.% of the obtained products was pressed into a toroidal-shaped mould with an outer diameter of 7 mm, an inner diameter of 3 mm, and a thickness of 2 mm for microwave measurement, with paraffin wax used as the binder. The electrical conductivity of the samples was tested by an RTS-9 model four-point probe.

3 Results and discussion

A series of experiments were carried out to determine the phase transition mechanism when varying the content of Co^{2+} added into the reaction solutions. In the SEM pattern (Fig. 1(a)), the undoped sample (C0) showed cabbage-like microspheres, which were assembled by MnO_2 nanosheets. The diameter of the microspheres was approximately 600 nm, and the average thickness of the nanosheets was approximately 15 nm. In the TEM image (Fig. S1 in the Electronic Supplementary Material (ESM)), the microspheres linked with each other to form irregular structures. The lattice fringes 0.35 and 0.24 nm corresponded to the interplanar spacing of (006) and (012) of δ-MnO_2, respectively [27]. Combining the FFT analyses and the XRD pattern (Fig. 1(b)), C0 can be assigned to the hexagonal δ-MnO_2 (JCPDS No. 86-0666). When Co^{2+} was added to the reaction solution, nanofibres appeared in the samples C2 (Fig. S2 in the ESM) and C4 (Fig. 1(b)), while XRD patterns could not capture the changes, it still indicated a δ phase with no impurity peaks. To identify the phase of the nanofibres, TEM was performed. In the TEM images of C4 (Fig. 3), the nanofibres had rough edges. The diameters of the nanofibres ranged from 20 to 50 nm, and several fibres tended to grow as bundles to reduce the surface energy. The corresponding FFT showed a single-crystal diffraction pattern and confirmed the results that the phase of the nanofibres was completely different from that of the nanosheets. The lattice fringes 0.48 and 0.27 nm of the nanofibres corresponded to the (200) and (101) planes of α-MnO_2, respectively [28]. According to the XRD patterns, α-MnO_2 in C2 and C4 were not detected, because the concentration of α-MnO_2 was below the detection limit of the instrument.

As Co increased, the content of nanowires continued to increase, and the shapes of the nanosheets tended to collapse and the α-MnO_2 was detected by XRD (Fig. 2, C6). When the doping content was increased to 8.5 mmol, the morphologies

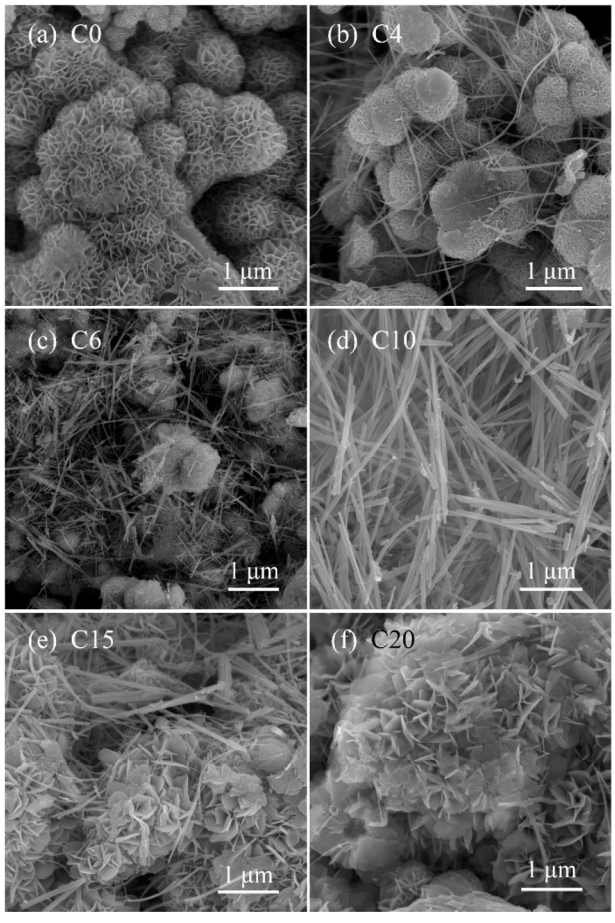

Figure 1 The SEM images of (a) C0, (b) C4, (c) C6, (d) C8.5, (e) C15, and (f) C20.

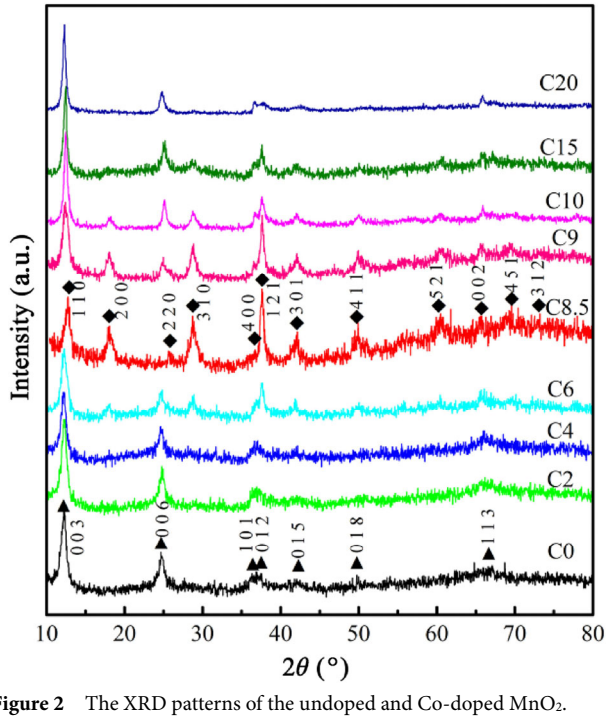

Figure 2 The XRD patterns of the undoped and Co-doped MnO_2.

were pure nanowires. The diameters of the nanowires were approximately 60 nm, which were thicker than the nanofibers (~ 20 nm) in previous samples. The nanowires were several micrometres in length and several of them assembled as bundles. The nanowires twisted with each other and formed trapping centres. The XRD pattern of C8.5 was assigned to

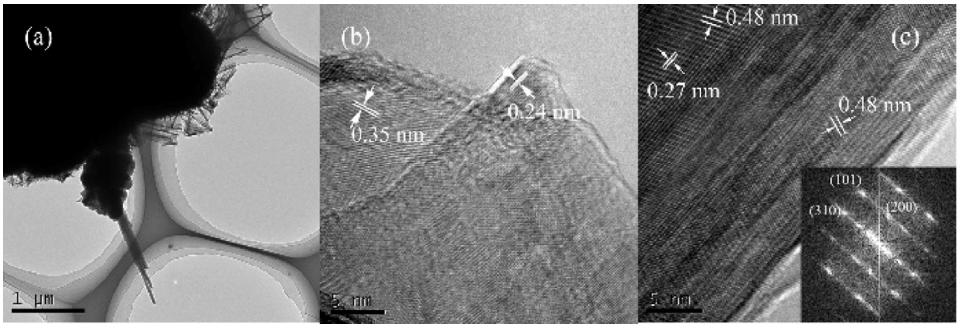

Figure 3 (a) The regular TEM image of C4. (b) HRTEM image of nanosheet in C4. (c) HRTEM image of nanofibres in C4 and the corresponding FFT.

α-MnO_2 phase (JCPDS No. 41-0141) [29]. With increasing Co^{2+} content, the number of nanowire structures decreased and the nanosheets no longer assembled as spheres but had a looser structure. According to the XRD results, C10 and C15 were still the mixture of the α and δ phases. When the doping content reached 20 mmol, rose-flower-like microspheres were assembled by a number of independent petal-nanosheets. From the XRD results, the peaks matched well with δ-MnO_2 with no extra peaks, and the intensities of the main peaks became stronger than C0, which indicated that C20 was pure δ-MnO_2 with good crystallization. The crystalline phase was transformed by changing the Co doping content.

When the doping content was larger than 8 mmol ($x > 8$), the microspheres composed of nanosheets were not assembled to be as compact as those in Cx ($x < 8$), which was due to the high ionic strength in the solutions. There was a different self-assembly mechanism in the two different conditions. Particles in low ionic strength solution realigned themselves and would not be fixed until they reached a low free energy state [30, 31]. In the course of the experiment, when more than 8.5 mmol $CoSO_4$ was added, the colour of the solution after the reaction was orange, which indicated that there was an amount of Co^{2+} ions in the solution. Therefore, in high Co^{2+} solutions, the nanosheets were fixed in the initial stage so that the microspheres could not obtain a compact structure. Fortunately, due to the incompact structure, there existed broken microspheres, which revealed the microspheres own hollow structures, as shown in Fig. 1(f), which was due to the Ostwald ripening process [32].

The results of XRD were combined (Fig. 2), and the variations in the nanowires were consistent with the content changes in α-MnO_2. The two peaks 18.1° and 28.7°, which corresponded to the α-MnO_2 phase, appeared in C6–C15, and the intensities of the peaks first increased and then decreased. The α-MnO_2 could not be detected clearly in C2 and C4 by XRD due to its low concentration. The phenomena of phase transition occurring, along with the amount of doping, are similar to those of the Ouroboros – the crystalline phase finally turns back to the starting point.

XPS was carried out to obtain information about the chemical state and composition of the surface situation of the samples. The samples of C4, C8.5 and C20 were subjected to the XPS test, and the results are shown in Fig. 4. In Fig. 4(b), the curves of Co were detected, which indicated that the metal ions had successfully doped into the MnO_2 crystal. The binding energies at 779.5 and 794.5 eV were assigned to Co^{3+}, and the binding energies at 780.4 and 795.3 eV were assigned to Co^{2+}. After analysis of the curves, nearly all the ions in C4 were Co^{3+}, and in C20, they were all Co^{2+} ions. In C8.5, the value of the Co 2p 3/2 peak was 779.9 eV, and the 2p 1/2 peak was 795.0 eV, which indicated there was a co-existence between Co(II) and Co(III) [33], and the Co^{2+} was not oxidized completely. The XPS spectra of O 1s are shown in Fig. 4(c). The binding energy of 529.7 eV was assigned to the lattice oxygen, and 531.1 eV was assigned to the surface adsorbed oxygen. As the Co ions doped into the MnO_2, the binding energy of O 1s moved to a higher value, which indicated that the Co^{2+} doping enhanced the stability of the MnO_2. Figure 4(d) shows the Mn 2p peaks from the samples. The spin-energy separation was 11.8 eV, which indicated the existence of MnO_2 [34]. The peaks at 642.6 and 641.3 eV were assigned to the surface ions of Mn^{4+} and Mn^{3+}, respectively. In C0 and C4, Mn^{2+} existed (the purple lines in Fig. 4), while in the high-doped samples, there was no peak for Mn^{2+}. Overall, the values of binding energy increased as the doping content increased, which represented a higher oxidation ability of Mn.

XRF was carried out to analyse the content of elements in the samples, and the results are shown in Table 1. As the Co content increased, the actual Co content in the samples increased. There was no obvious correlation between the decrease in Mn content and the increase in Co content. There was no evidence that Co ions replaced the Mn in the MnO_2, and combined with our previous work, the more favourable doping positions were in the (2 × 2) tunnels of the α-MnO_2 or the interlayer of δ-MnO_2 [35]. Among the samples, the content of Mn was regarded as a constant, and the relative contents of K were described as the value of K/Mn. As the increases of Co content, the relative content of K decreased firstly and then increased, and reached the lowest point for C8.5. Because C8.5 was pure α-MnO_2 with the tunnel structure where limited doping sites existed, as the Co doped, doping sites left for K became fewer which resulted in the lowest content of K in C8.5 among the

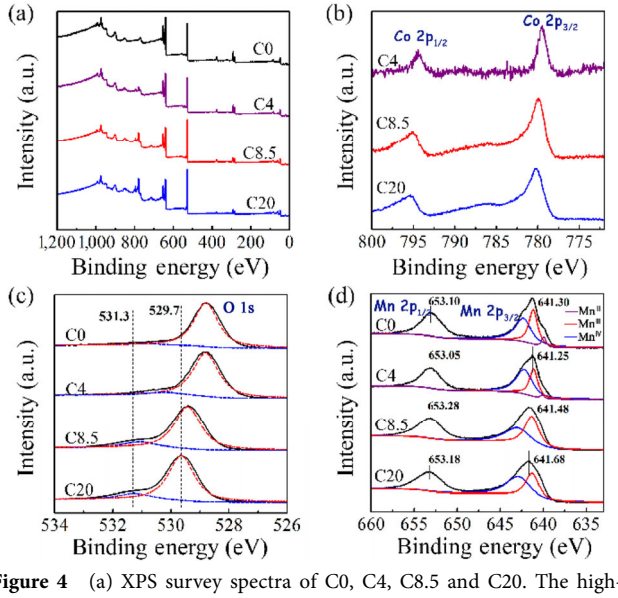

Figure 4 (a) XPS survey spectra of C0, C4, C8.5 and C20. The high-resolution XPS spectra for the element (b) Co 2p, (c) O 1s and (d) Mn 2p of C0, C4, C8.5 and C20.

Table 1 XRF analysis results of C0, C4, C8.5, C12 and C20, where the major elements are the Mn, O, K and Co doping ions

Sample	Mn (%)	O (%)	K (%)	Co (%)	K/Mn
C0	35.00	54.30	10.70		0.31
C4	32.05	53.76	10.03	4.16	0.31
C8.5	32.14	53.22	6.12	8.52	0.19
C12	30.70	51.75	6.85	10.70	0.22
C20	30.46	48.13	8.28	13.13	0.27

samples. With an increased Co content, the contents of K and Co both increased. These results demonstrated that δ-MnO_2 contained more doped ions than α-MnO_2.

To obtain the expected products, it was important to determine the growth mechanism of Co-doped MnO_2. Figure 5 is a schematic illustration of the crystal forms and morphological changes. In reaction solution, $KMnO_4$ oxidized Co^{2+} to Co^{3+}, and $KMnO_2$ was reduced to {MnO_x}. The Co^{3+} could not exist as ions in the aqueous solution, so the complexation reaction occurred, and a complex of Co^{3+}{MnO_x}$_4$ formed. In the complex, the Co^{3+} ions were four-coordinated in a square planar. The complex formed the 2 × 2 tunnel structure, and Co ions occupied the centre of the tunnel. Based on the complex, Co^{3+} ions were used as permanent templates, and the crystal then grew in the c direction, which generated α-MnO_2. When the doping content was low, the cobalt ions enrichment zone formed α-MnO_2, and the samples showed a mixture of nanofibre-α-MnO_2 and nanosheet-δ-MnO_2. When the appropriate amount of Co^{2+} was added to the solution, 8.5 mmol, the products were α-MnO_2.

When the Co^{2+} ions were excessive, there was not enough oxygen to oxidize all of the Co^{2+}. In addition, Co^{3+} ions could not stably exist in the aqueous solution, and the complex Co^{3+}{MnO_x}$_4$ became unstable; instead, the complex with Co^{2+} as the centre was generated. A great deal of complex centred on Co^{2+} existed in the solution and compared to the Co^{3+}-O, the Co^{2+}-O bonds had longer bond lengths. On the other hand, to take up more Co^{2+} ions, the complexes chose to connect side by side, the 1 × 1 tunnel structures were destroyed, and the (MnO_6) turned to be arranged in a lamellar form. In the perfect crystal, the square edge length of the tunnel section was 3.610 Å in α-MnO_2, while in δ-MnO_2, the distance between O from the adjacent layer was 5.051 Å, and the variation was nearly 40%. The longer bond length of Co^{2+}-O, compared to that of Co^{3+}-O, was one of the main factors. According to the XRD, the (003) and (006) peaks of C20 moved towards the right side slightly and pointed to a higher 2θ than C0, which indicated that the doped δ-MnO_2 had narrower interlayer spacing (Table 2). In our previous research, Co-doped δ-MnO_2 was explored by theoretical calculation, where Co doping was proven to decrease the lattice constant in the *c*-axis [35]. The doped Co contracted the crystal by pulling the lattice O so that there were decreases in the *c*-axis of the crystal. At the same time, this contraction made it possible for α to transform into the δ form. On the other hand, the layered structure of δ-MnO_2 made it possible to carry more ions. Therefore, the nanowires began to collapse and generated layer-form structures with excessive cobalt ions. As the doping content increased, the nanowires decreased until they disappeared. In contrast to pure δ-MnO_2, the interlayer ions of new δ-MnO_2 were K^+ ions and Co^{2+} ions.

With the combined experimental results, the mechanism of phase transition can be explained as follows. The Co^{2+} ions in the reaction solution controlled the growth of MnO_2. Adding the proper content of Co^{2+} (8.5 mmol), Co^{2+} was oxidized by $KMnO_4$ and generated Co^{3+}, and then the Co^{3+} acted as a template to form α-MnO_2. Due to the instability of Co^{3+}, when excessive Co^{2+} (20 mmol) was added to the solution, Co^{3+} ions were replaced by Co^{2+}, and the structure of the Co^{3+}{MnO_x}$_4$ complex collapsed; thus, the α-MnO_2 became the unstable structure, and the δ-MnO_2 with Co^{2+} in the interlayers became the stable structure again. During the nodes, the products were a mixture of δ- and α-MnO_2, and its proportion was controlled by the Co^{2+} content.

Table 2 The *d*(003) and *d*(006) of C0, C20

	d(003)	*d*(006)
C0	7.2945 Å	3.5925 Å
C20	7.1798 Å	3.5819 Å

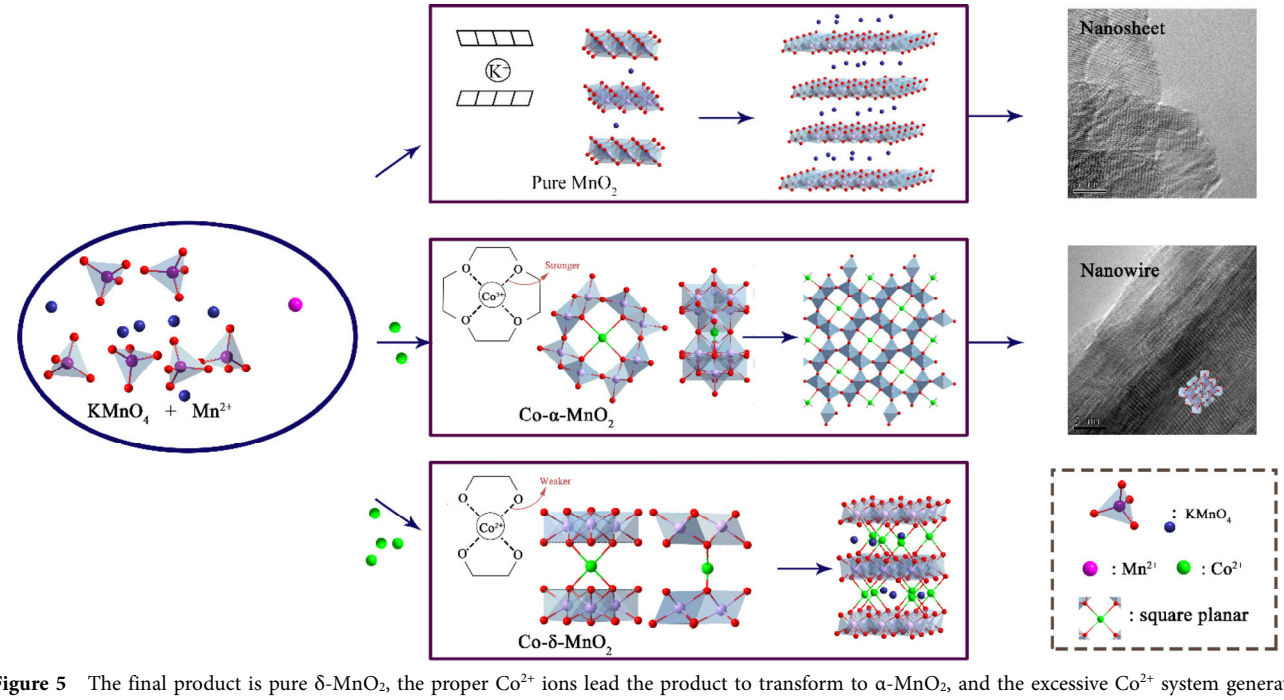

Figure 5 The final product is pure δ-MnO_2, the proper Co^{2+} ions lead the product to transform to α-MnO_2, and the excessive Co^{2+} system generates Co-δ-MnO_2.

From a previous report, α-MnO_2 always showed a high RL but a narrow effective bandwidth (EB) due to a low impedance matching performance [6, 22]. The nanosheets of δ-MnO_2 that were assembled by nanosheets were an excellent morphology for absorbance [36]. The lamellar structure of δ-MnO_2 contained more doped magnetic ions, which was beneficial to enhanced magnetic loss and improved impedance matching, but the dielectric performance of δ-MnO_2 was poor. Therefore, a composite of α-MnO_2 and δ-MnO_2 was expected to incorporate both merits to generate a great absorber. Meanwhile, the proportion of α-MnO_2 and δ-MnO_2 was adjusted by the Co doping content. The samples were mixed with wax to form composites via a hot-press process, and their absorbing properties were tested. The filler loading ratios of samples were 50 wt.% for all samples. To investigate the electromagnetic absorption properties, the RL of the samples were calculated by the transmit line theory

$$\mathrm{RL} = 20\log\left|\frac{Z_{\mathrm{in}}-1}{Z_{\mathrm{in}}+1}\right| \quad (1)$$

$$Z_{\mathrm{in}} = \sqrt{\frac{\mu_{\mathrm{r}}}{\varepsilon_{\mathrm{r}}}}\tanh\left(j\frac{2\pi fd}{c}\sqrt{\mu_{\mathrm{r}}\varepsilon_{\mathrm{r}}}\right) \quad (2)$$

where Z_{in} is the normalized input impedance, ε_{r} is the complex permittivity, μ_{r} is the complex permeability, d is the thickness of the absorbing layers, and c is the velocity of light in free space. The 3D plots of the RL of samples vs. the frequency and thickness are shown in Fig. 6. The absorptive capacities of the samples are shown in blue, and darker colours represent high performance. When the RL value was lower than −10 dB, it indicated that the sample can eliminate 90% electromagnetic wave, which is generally defined as effective absorbing, the

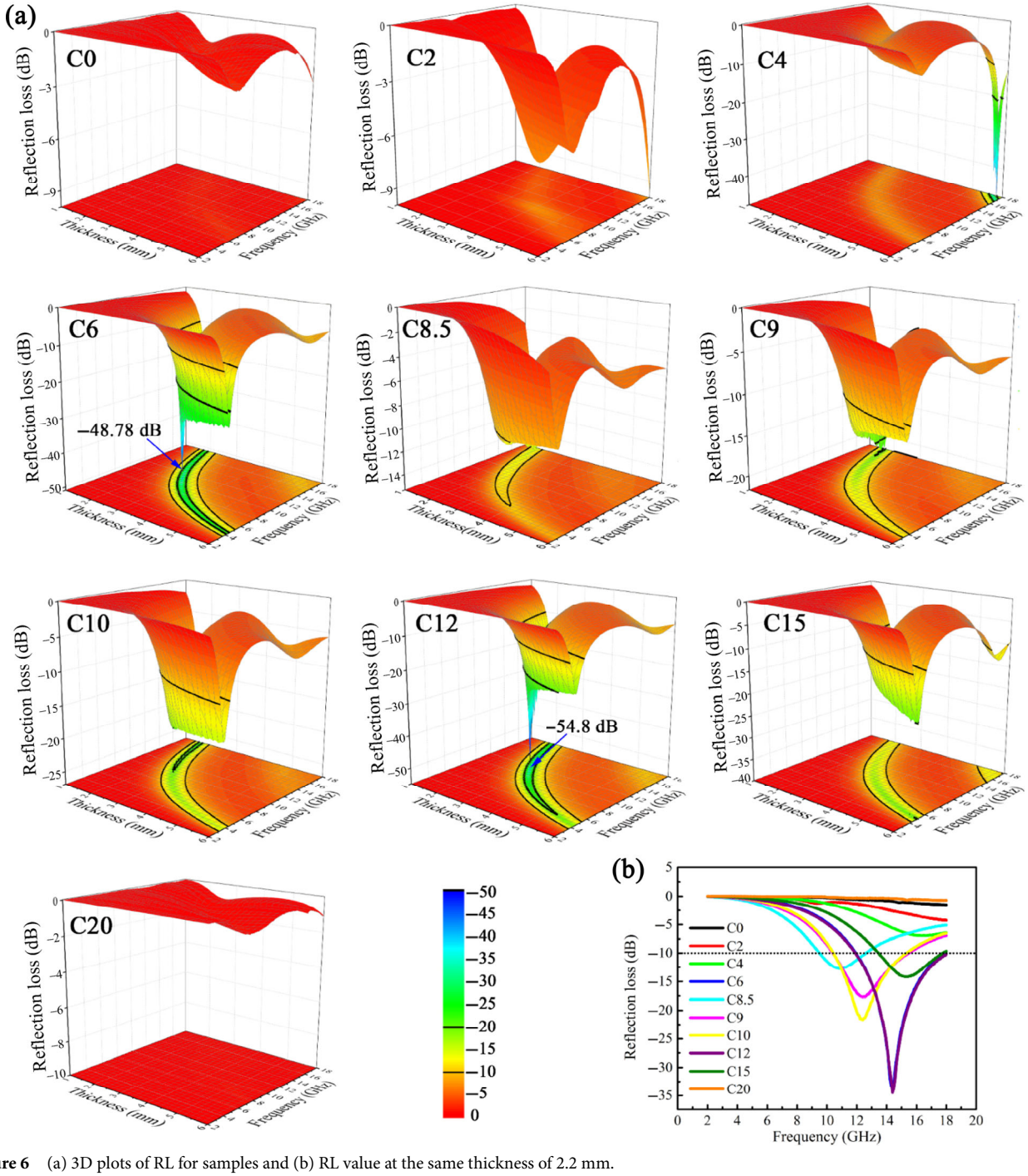

Figure 6 (a) 3D plots of RL for samples and (b) RL value at the same thickness of 2.2 mm.

bandwidth in which the RL value of every point maintains lower than −10 dB is called effective microwave absorbing bandwidth [36–40]. A proper absorber demands low RL value and broad EB with a thin thickness. As shown in Fig. 6, the samples C0, C2 and C20 could not achieve effective absorption within the scope of the study (2–18 GHz, 1–6 mm). The other samples achieved effective absorption at 2–18 GHz. Considering the maximum RL and EB (Fig. S3 in the ESM), the performance of the samples was first improved and then worsened as the doping content increased.

Figure 7 shows 2D images of the samples that can reach the effective absorbing value (RL < −10 dB) in the frequency range (2–18 GHz), with thicknesses in the range of 1.0–6.0 mm. As the thickness increased, the absorption peak moved to a lower frequency. The relationship between frequency with the maximum RL value and its matching thickness obeys the quarter-wavelength equation

$$t_m = \frac{n\lambda}{4} = \frac{nc}{4f_m\left(|\varepsilon_r||\mu_r|\right)^{1/2}} \quad (n = 1,3,5\cdots) \tag{3}$$

Where t_m is the thickness of absorber, f_m is the peak frequency, λ is the wavelength at f_m. ε_r and μ_r are the complex permittivity and permeability at f_m. For a single-layer microwave absorber, interference cancellation would occur at the corresponding thicknesses, as a result, that would usually cause lower RL values. The simulated thicknesses are shown as violet lines in Fig. 7 and agreed well with the calculated results. The maximum RL of C6 was −48.78 dB, it achieved effective absorbance in the Ku band with a 2.2 mm thickness. The maximum RL of C8.5 was −15.37 dB, and the maximum EB of C8.5 was 5.12 GHz from 12.88 to 18 GHz. The EB of C10 was 5.92 GHz from 12.08 to 18 GHz, with a 2 mm thickness. For C12, the maximum value of RL was −54.8 dB at 11.44 GHz with a thickness of 2.7 mm; it also realized effective absorption in the Ku band at a thickness of 2.2 mm and in the X band at a thickness of 3.1 mm. Overall, C6 and C12 showed the best performance and reached effective absorption in the Ku and X bands, which indicated that the composites of α-MnO_2 and δ-MnO_2 had better absorbing ability than a single phase. From Fig. 6(b), at the same thickness, as increases of Co doping the matching frequencies of samples shifted to the lower frequency firstly and then to the higher frequency, which were determined by the changes of electromagnetic parameters.

To determine the absorption mechanisms of the samples, the complex permittivity ($\varepsilon_r = \varepsilon' - j\varepsilon''$) and complex permeability ($\mu_r = \mu' - j\mu''$) were investigated carefully. The real part (ε', μ') and imaginary part (ε'', μ'') values presented the capability of storing and dissipating the electromagnetic energy, respectively. Figure 8 shows the complex permittivity of samples over 2–18 GHz with 50 wt.% filler loading ratios. For complex permittivity, the values exhibited declines in the whole frequency range because of the dispersion response. Overall, the value of pure δ-MnO_2 had the lowest value of ε' and ε'', and sample C8.5 had the highest ε' and ε'' among all samples. The dielectric loss factors ($\tan\delta_\varepsilon$) were used to evaluate the loss capacity [41], as shown in Fig. 8(c), and all samples had three peaks at ~ 3.52, ~ 9.69, and ~ 15 GHz. The values of complex permittivity decreased in the order C8.5 > C9 > C10 > C6 ≈ C12 > C15. Therefore, the values of ε' and ε'' were in direct proportion to the ratio of α-MnO_2 in the samples. It was known that the dielectric loss was contributed in two parts, relaxation loss and conductance loss. Dipolar polarization resulted from the behaviour of permanent dipoles under the electromagnetic field

$$\varepsilon_r = \varepsilon_\infty + \frac{\varepsilon_s - \varepsilon_\infty}{1 + j2\pi f\tau} = \varepsilon' - j\varepsilon'' \tag{4}$$

Debye dipolar polarization can be expressed by Eq. (4), where ε_s and ε_∞ are the static permittivity and relative dielectric permittivity at the high-frequency limit, respectively; τ is the relaxation time; and f is the frequency. The ε' and ε'' can be described by

$$\varepsilon' = \varepsilon_\infty + \frac{\varepsilon_s - \varepsilon_\infty}{1 + (2\pi f)^2\tau^2} \tag{5}$$

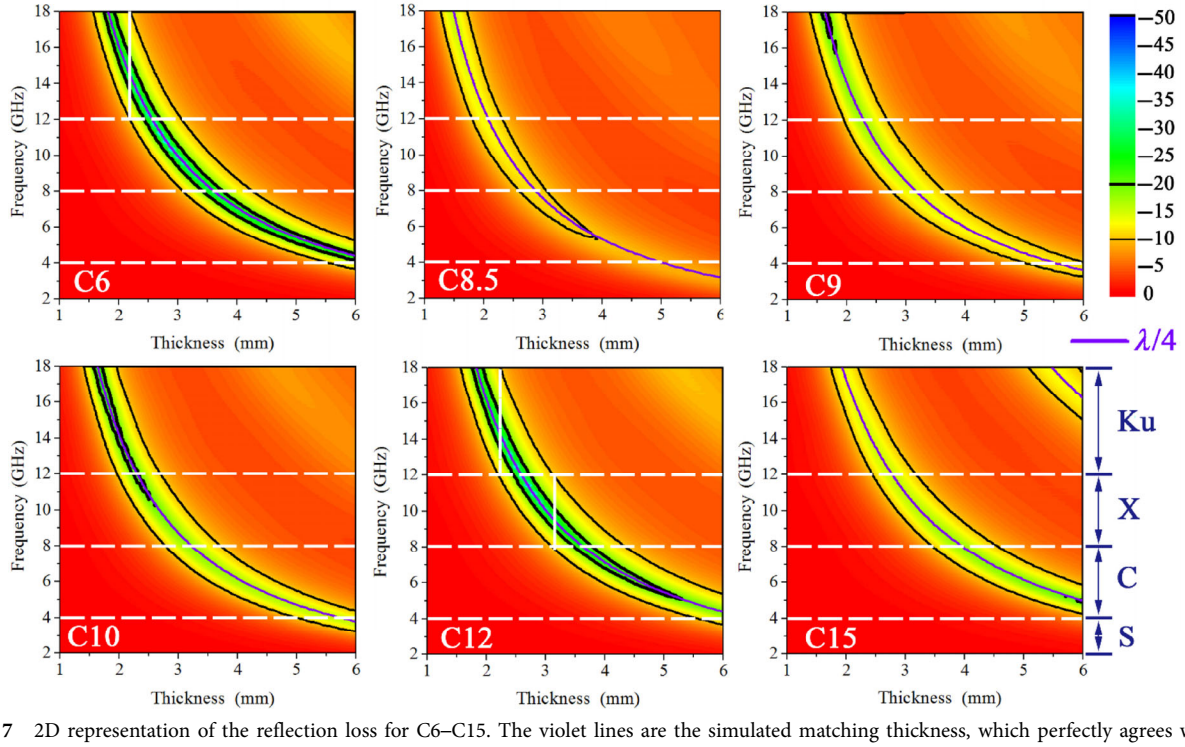

Figure 7 2D representation of the reflection loss for C6–C15. The violet lines are the simulated matching thickness, which perfectly agrees with the calculation results.

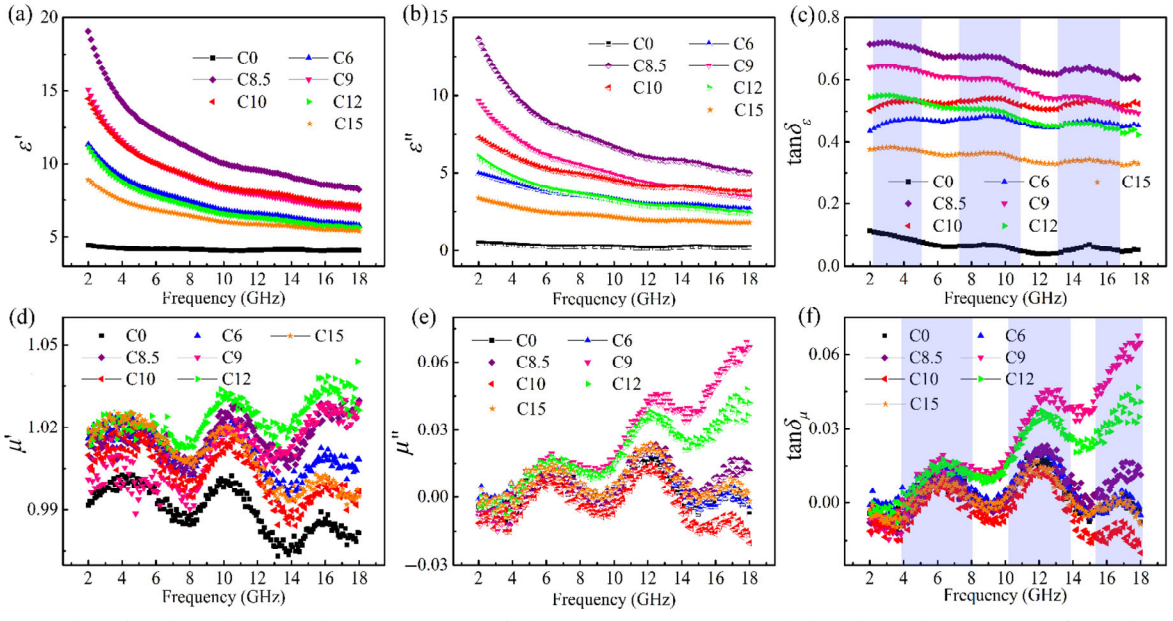

Figure 8 The plots of (a) the real parts, (b) the imaginary parts of relative complex permittivity, (c) the dielectric loss tangent (tanδ_ε), (d) the real parts, (e) the imaginary parts of relative complex permeability, and (f) the magnetic loss tangent versus frequency (tanδ_μ) with 50 wt.% filler loading ratios.

$$\varepsilon'' = \frac{2\pi f\tau(\varepsilon_s - \varepsilon_\infty)}{1+(2\pi f)^2\tau^2} \quad (6)$$

According to Eqs. (5) and (6), the relationship between ε' and ε'' can be obtained

$$\left[\varepsilon' - \frac{1}{2}(\varepsilon_s + \varepsilon_\infty)\right]^2 + (\varepsilon'')^2 = \frac{1}{4}(\varepsilon_s - \varepsilon_\infty)^2 \quad (7)$$

Based on Eq. (7), the curve of ε' versus ε'' would form a semicircle when there is a Debye relaxation process. The semicircle is also called the Cole-Cole semicircle, and the plot of ε' versus ε'' is called the Cole-Cole figure [42, 43]. The Cole-Cole figures of the samples are shown in Fig. S4 in the ESM. All samples had three semicircles that were consistent with the three peaks of tan δ_ε and indicated that α-MnO_2 had no new relaxation process compared with δ-MnO_2. The increases in Debye relaxation were mainly due to the stronger dipolar polarization of α-MnO_2.

According to the free-electron theory, high electrical conductivity caused high conductance loss. The electrical conductivities of the samples were detected by an RTS-9 model four-point probe. The results are shown in Fig. S5 in the ESM. The conductivity reached the highest value at C8.5, which showed a positive correlation between the share of α-MnO_2 and the conductivities of the samples. This correlation also indicated that the increases in conductivities of the samples were due to the generation of α-MnO_2. The conductivities were mainly derived from two parts, migrating electrons and hopping electrons, and the crystal form was the main factor that affected the conductivities [44]. The nanowires of α-MnO_2 had a larger aspect ratio and twisted with each other to form a conductive network [38, 45]. On the other hand, the low valence state of Mn had a negative effect on electrical conductivity, while Mn showed a higher valence in α-MnO_2 (Fig. 4).

As for the complex permeability of the samples (Figs. 8(d)–8(f)), due to MnO_2 was a nonmagnetic material, all the μ' were almost 1 and the μ'' were close to 0, the contribution from complex permeability was limited. Therefore, it does not merit any addition discussion here [46, 47].

The C0 and C20 samples are both δ phase, although C20 contained Co ions, therefore, they had different morphologies. There must result in some differences in the electromagnetic parameters of C0 and C20, and the results are shown in Fig. S6 in the ESM. The filler loading ratios were 50 wt.%. The complex permittivity of C20 was lower than that of C0, which indicated that Co-doped δ-MnO_2 could not increase the dielectric performance, and the increased permittivity above was caused by the generation of the α phase. The morphology of C20 was looser than that of C0, and the poor dielectric performance indicated that the rose-flower-like structure was not a proper structure for absorbers. In view of the crystal structure, Co doped into δ-MnO_2 decreased the average bond length and increased the bond energy of Mn-O, which weakened the dielectric response to the electromagnetic field [35]. For magnetic performance, the real parts of permeability of C20 were higher than those of C0, and the imaginary parts had no obvious difference. Therefore, the main effects of Co doping increased the real parts of permeability.

Compared with other samples, C8.5 had the highest electromagnetic parameter values but could not always show the best absorbing performance. For the absorber, high microwave attenuation and proper impedance matching were two important factors [48]. The attenuation constant and impedance matching ratio were used to measure these two factors. The attenuation constant α of the samples is calculated by Eq. (8)

$$\alpha = \frac{\sqrt{2}\pi f}{c}\sqrt{(\mu''\varepsilon\mu'' - \mu'\varepsilon' + \sqrt{(\mu''\varepsilon'' - \mu'\varepsilon')^2 + (\mu'\varepsilon'' + \mu''\varepsilon')^2}} \quad (8)$$

The values of α represented the attenuation capability of the samples; the higher the value is, the stronger the absorption. As shown in Fig. 9(a), the attenuation constant α exhibited an enhanced tendency with increasing frequency for all samples. There was a positive correlation between the attenuation ability and share of α-MnO_2, and C8.5 had the largest attenuation ability. The impedance matching ratio is calculated and shown in Fig. 9(b). To allow incident microwaves to enter the absorber with little reflection, the matching ratio should be greater than 0.3 [18]. The higher ratio ensures that more electromagnetic waves can propagate into the absorber so that

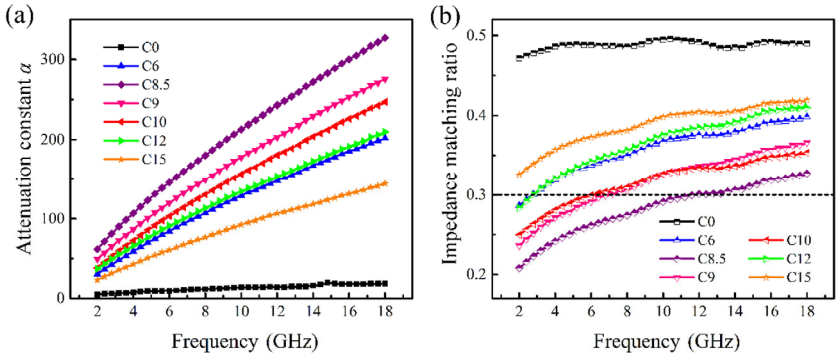

Figure 9 Attenuation constant α (a) and impedance matching ratios (b).

the absorber can play a role in processing the electromagnetic energy into other forms of energy [49]. As the doping content increased, the complex permittivity of the samples increased, and the complex permeability had no obvious increase; thus, the samples showed worse impedance matching ratios. It can be seen from Fig. 9(b) that C8.5 was way off the impedance matching, so the absorbing performance was poor. The synergistic effects of α- and δ-MnO_2 played an important role in helping the samples obtain impedance matching. The C6 and C12 samples exhibited the perfect combination of the attenuation and impedance matching constant. As a result, C6 and C12 had the best performance.

In the mixture of δ-/α-MnO_2 composites, microwave propagation occurred in both crystal forms. The main absorption mechanism of the microwave was summarized by three factors. First, the nanowires of α-MnO_2 distributed randomly and entwined with each other in the samples to form trapping centres. The nanosheets of δ-MnO_2 formed by multiple nanosheets caused multiple reflections and scattering of microwaves. Second, the values of conductivities were in direct proportion to the α-MnO_2 content, and the higher conductivities brought higher conductance loss. At the same time, the interface among nanowires, nanosheets and nanowires and the powders and wax caused Maxwell-Wagner relaxation. Under the action of the electromagnetic field, the electrons migrated, and these movements were blocked by the interfaces. The interfaces with concentrated electrons were equivalent to capacitors [50]. In the electromagnetic field, capacitors transformed the electromagnetic energy to other energies. During usage, it was necessary to synthetically consider the influence of impedance matching, attenuation characteristics and absorber thickness to adapt the service conditions, and all these factors were satisfied by electing an appropriate doping content.

The other reported electromagnetic wave absorbing performance of MnO_2 materials in recent literatures were summarized in Table 3. By contrast, the composites of δ-/α-MnO_2 with Co^{2+} doping showed superior absorption ability and broader effective absorption bandwidth, indicating their promising prospect as a kind of broadband absorbing material.

Table 3 Microwave absorption performance of MnO_2

Filler	Loading ratio (wt.%)[a]	RL (dB)	Thickness (mm)	EB (GHz)	Ref.
C6	50	−48.78	2.2	6.00	Herein
C12	50	−54.8	2.2	6.08	Herein
α-MnO_2	50	−41.0	1.6	~ 2.30	[6]
β-MnO_2	50	−25.5	1.5	5.00	[51]
Hollow α-MnO_2	50	−40.0	4	3.50	[5]
MnO_2/RGO	50	−37.0	2	4.50	[47]
δ-/α-MnO_2	40	−45.2	2	3.60	[52]
Fe_3O_4@MnO_2	50	−48.5	2	3.20	[53]

[a]The matrixes were all wax.

4 Conclusion

The mechanism of the phase transition circle caused by Co doping was completely explored. A new idea was provided about controlling the growth of MnO_2 nanostructures and phases. The mixture of δ-MnO_2 nanosheets and α-MnO_2 nanowires on the microscopic scale influenced the microwave absorbing performance. By controlling the phase transformation process and regulating the two-phase composition, the controllable preparation of the same material with different phases was achieved, and the wave-absorbing performance was effectively optimized. Several samples with different Co doping contents realized effective absorbing (< 10 dB), with a wide frequency at low thickness. Co-controlled δ-/α-MnO_2 may not only become an excellent electromagnetic absorbance material but also have great potential in other fields.

Acknowledgements

The authors acknowledge the Support by Program for the National Natural Science Foundation of China (Nos. 51577021 and U1704253), and the Fundamental Research Funds for the Central Universities (No. DUT17GF107).

Electronic Supplementary Material: Supplementary material (further details of the characterization and performance including SEM, TEM, Cole-Cole patterns, electrical conductivity, etc.) is available in the online version of this article at https://doi.org/10.1007/s12274-019-2578-2.

References

[1] Yuan, Y. F.; Nie, A. M.; Odegard, G. M.; Xu, R.; Zhou, D. H.; Santhanagopalan, S.; He, K.; Asayesh-Ardakani, H.; Meng, D. D.; Klie, R. F. et al. Asynchronous crystal cell expansion during lithiation of K^+-Stabilized α-MnO_2. *Nano Lett.* **2015**, *15*, 2998–3007.

[2] Li, Y. Q.; Shi, X. M.; Lang, X. Y.; Wen, Z.; Li, J. C.; Jiang, Q. Remarkable improvements in volumetric energy and power of 3D MnO_2 microsupercapacitors by tuning crystallographic structures. *Adv. Funct. Mater.* **2016**, *26*, 1830–1839.

[3] Liu, P. B.; Zhu, Y. D.; Gao, X. G.; Huang, Y.; Wang, Y.; Qin, S. Y.; Zhang, Y. Q. Rational construction of bowl-like MnO_2 nanosheets with excellent electrochemical performance for supercapacitor electrodes. *Chem. Eng. J.* **2018**, *350*, 79–88.

[4] Ren, H.; Zhao, J.; Yang, L.; Liang, Q. H.; Madhavi, S.; Yan, Q. Y. Inverse opal manganese dioxide constructed by few-layered ultrathin nanosheets as high-performance cathodes for aqueous zinc-ion batteries. *Nano Res.* **2019**, *12*, 1347–1353.

[5] Wang, Y.; Han, B. Q.; Chen, N.; Deng, D. Y.; Guan, H. T.; Wang, Y.

D. Enhanced microwave absorption properties of MnO_2 hollow microspheres consisted of MnO_2 nanoribbons synthesized by a facile hydrothermal method. *J. Alloys Compd*. **2016**, *676*, 224–230.

[6] Zhou, M.; Zhang, X.; Wei, J. M.; Zhao, S. L.; Wang, L.; Feng, B. X. Morphology-controlled synthesis and novel microwave absorption properties of hollow urchinlike α-MnO_2 nanostructures. *J. Phys. Chem. C* **2011**, *115*, 1398–1402.

[7] Xing, X. B.; Lv, G. C.; Xu, W.; Liao, L. B.; Jiang, W. T.; Li, Z. H.; Wang, G. S. Controllable adjustment of the crystal symmetry of K–MnO_2 and its influence on the frequency of microwave absorption. *RSC Adv*. **2016**, *6*, 58844–58853.

[8] Sikam, P.; Moontragoon, P.; Sararat, C.; Karaphun, A.; Swatsitang, E.; Pinitsoontorn, S.; Thongbai, P. DFT calculation and experimental study on structural, optical and magnetic properties of Co-doped $SrTiO_3$. *Appl. Surf. Sci*. **2018**, *446*, 92–113.

[9] Kang, J. L.; Hirata, A.; Kang, L. J.; Zhang, X. M.; Hou, Y.; Chen, L. Y.; Li, C.; Fujita, T.; Akagi, K.; Chen, M. W. Enhanced supercapacitor performance of MnO_2 by atomic doping. *Angew. Chem., Int. Ed*. **2013**, *52*, 1664–1667.

[10] Ye, Z. G.; Li, T.; Ma, G.; Dong, Y. H.; Zhou, X. L. Metal-ion (Fe, V, Co, and Ni)-Doped MnO_2 ultrathin nanosheets supported on carbon fiber paper for the oxygen evolution reaction. *Adv. Funct. Mater*. **2017**, *27*, 1704083.

[11] Sun, Q.; Liu, C.; Alves, M. E.; Ata-Ul-Karim, S. T.; Zhou, D. M.; He, J. Z.; Cui, P. X.; Wang, Y. J. The oxidation and sorption mechanism of Sb on δ-MnO_2. *Chem. Eng. J*. **2018**, *342*, 429–437.

[12] Guan, H. T.; Wang, Y.; Dong, C. J.; Chen, G.; Xiao, X. C.; Wang, Y. D. A novel microwave absorption material of Ni doped cryptomelane type manganese oxides. *Ceram. Int*. **2015**, *41*, 5688–5695.

[13] Agrawal, S.; Parveen, A.; Azam, A. Microwave assisted synthesis of Co doped NiO nanoparticles and its fluorescence properties. *J. Lumin*. **2017**, *184*, 250–255.

[14] Staniland, S.; Williams, W.; Telling, N.; Van Der Laan, G.; Harrison, A.; Ward, B. Controlled cobalt doping of magnetosomes *in vivo*. *Nat. Nanotechnol*. **2008**, *3*, 158–162.

[15] Huang, X. G.; Zhang, M. J.; Qin, Y. S.; Chen, Y. Y. Bead-like Co-doped ZnO with improved microwave absorption properties. *Ceram. Int*. **2019**, *45*, 7789–7796.

[16] Ahamed, I.; Pathak, R.; Skomski, R.; Kashyap, A. Magnetocrystalline anisotropy of ε-Fe_2O_3. *AIP Adv*. **2018**, *8*, 055815.

[17] Tang, C. L.; Wei, X.; Jiang, Y. M.; Wu, X. Y.; Han, L. N.; Wang, K. X.; Chen, J. S. Cobalt-doped MnO_2 hierarchical yolk–shell spheres with improved supercapacitive performance. *J. Phys. Chem. C* **2015**, *119*, 8465–8471.

[18] Liu, P. J.; Yao, Z. J.; Zhou, J. T.; Yang, Z. H.; Kong, L. B. Small magnetic Co-doped NiZn ferrite/graphene nanocomposites and their dual-region microwave absorption performance. *J. Mater. Chem. C* **2016**, *4*, 9738–9749.

[19] Yan, L. J.; Niu, L. Y.; Shen, C.; Zhang, Z. K.; Lin, J. H.; Shen, F. Y.; Gong, Y. Y.; Li, C.; Liu, X. J.; Xu, S. Q. Modulating the electronic structure and pseudocapacitance of δ-MnO_2 through transitional metal M (M = Fe, Co and Ni) doping. *Electrochim. Acta* **2019**, *306*, 529–540.

[20] Lv, G. C.; Xing, X. B.; Wu, L. M.; Jiang, W. T.; Li, Z. H.; Liao, L. B. Tunable high-performance microwave absorption for manganese dioxides by one-step Co doping modification. *Sci. Rep*. **2016**, *6*, 37400.

[21] Zhao, P. F.; Liang, C. Y.; Gong, X. W.; Gao, R.; Liu, J. W.; Wang, M.; Che, R. C. Microwave absorption enhancement, magnetic coupling and *ab initio* electronic structure of monodispersed $(Mn_{1-x}Co_x)_3O_4$ nanoparticles. *Nanoscale* **2013**, *5*, 8022–8028.

[22] Duan, Y. P.; Liu, Z.; Jing, H.; Zhang, Y. H.; Li, S. Q. Novel microwave dielectric response of Ni/Co-doped manganese dioxides and their microwave absorbing properties. *J. Mater. Chem*. **2012**, *22*, 18291–18299.

[23] Wang, J. W.; Chen, Y.; Chen, B. Z. Effects of transition-metal ions on the morphology and electrochemical properties of δ-MnO_2 for supercapacitors. *Met. Mater. Int*. **2014**, *20*, 989–996.

[24] Xie, Y. J.; Yu, Y. Y.; Gong, X. Q.; Guo, Y.; Guo, Y. L.; Wang, Y. Q.; Lu, G. Z. Effect of the crystal plane figure on the catalytic performance of MnO_2 for the total oxidation of propane. *CrystEngComm* **2015**, *17*, 3005–3014.

[25] Wang, C.; Liu, Y.; Feng, X.; Zhou, C. Y.; Liu, Y. L.; Yu, X.; Zhao, G. J. Phase regulation strategy of perovskite nanocrystals from 1D orthomorphic NH_4PbI_3 to 3D cubic $(NH_4)_{0.5}Cs_{0.5}pb(I_{0.5}Br_{0.5})_3$ phase enhances photoluminescence. *Angew. Chem., Int. Ed*. **2019**, *58*, 11642–11646.

[26] Sun, G. B.; Dong, B. X.; Cao, M. H.; Wei, B. Q.; Hu, C. W. Hierarchical dendrite-like magnetic materials of Fe_3O_4, γ-Fe_2O_3, and Fe with high performance of microwave absorption. *Chem. Mater*. **2011**, *23*, 1587–1593.

[27] Devaraj, S.; Munichandraiah, N. Effect of crystallographic structure of MnO_2 on its electrochemical capacitance properties. *J. Phys. Chem. C* **2008**, *112*, 4406–4417.

[28] Yuan, Y. F.; Wood, S. M.; He, K.; Yao, W. T.; Tompsett, D.; Lu, J.; Nie, A. M.; Islam, M. S.; Shahbazian-Yassar, R. Atomistic insights into the oriented attachment of tunnel-based oxide nanostructures. *ACS Nano* **2016**, *10*, 539–548.

[29] Li, Y. L.; Wang, J. J.; Zhang, Y.; Banis, M. N.; Liu, J.; Geng, D. S.; Li, R. Y.; Sun, X. L. Facile controlled synthesis and growth mechanisms of flower-like and tubular MnO_2 nanostructures by microwave-assisted hydrothermal method. *J. Colloid Interface Sci*. **2012**, *369*, 123–128.

[30] Collier, A. P.; Hetherington, C. J. D.; Hounslow, M. J. Alignment mechanisms between particles in crystalline aggregates. *J. Cryst. Growth* **2000**, *208*, 513–519.

[31] Li, J.; Hietala, S.; Tian, X. L. $BaTiO_3$ supercages: Unusual oriented nanoparticle aggregation and continuous ordering transition in morphology. *ACS Nano* **2015**, *9*, 496–502.

[32] Yec, C. C.; Zeng, H. C. Synthesis of complex nanomaterials via Ostwald ripening. *J. Mater. Chem. A* **2014**, *2*, 4843–4851.

[33] Li, X.; Wang, L.; You, W. B.; Xing, L. S.; Yu, X. F.; Li, Y. S.; Che, R. C. Morphology-controlled synthesis and excellent microwave absorption performance of $ZnCo_2O_4$ nanostructures via a self-assembly process of flake units. *Nanoscale* **2019**, *11*, 2694–2702.

[34] Peng, R. C.; Wu, N.; Zheng, Y.; Huang, Y. B.; Luo, Y. B.; Yu, P.; Zhuang, L. Large-scale synthesis of metal-ion-doped manganese dioxide for enhanced electrochemical performance. *ACS Appl. Mater. Interfaces* **2016**, *8*, 8474–8480.

[35] Song, L. L.; Duan, Y. P.; Zhang, Y. H.; Wang, T.M. Promoting defect formation and microwave loss properties in δ-MnO_2 via Co doping: A first-principles study. *Comput. Mater. Sci*. **2017**, *138*, 288–294.

[36] Zhang, Y. L.; Wang, X. X.; Cao, M. S. Confinedly implanted $NiFe_2O_4$-rGO: Cluster tailoring and highly tunable electromagnetic properties for selective-frequency microwave absorption. *Nano Res*. **2018**, *11*, 1426–1436.

[37] Wang, L.; Li, X.; Li, Q. Q.; Zhao, Y. H.; Che, R. C. Enhanced polarization from hollow cube-like $ZnSnO_3$ wrapped by multiwalled carbon nanotubes: As a lightweight and high-performance microwave absorber. *ACS Appl. Mater. Interfaces* **2018**, *10*, 22602–22610.

[38] Singh, S. K.; Akhtar, M. J.; Kar, K. K. Hierarchical carbon nanotube-coated carbon fiber: Ultra lightweight, thin, and highly efficient microwave absorber. *ACS Appl. Mater. Interfaces* **2018**, *10*, 24816–24828.

[39] Zhang, M. M.; Jiang, Z. Y.; Lv, X. Y.; Zhang, X. F.; Zhang, Y. H.; Zhang, J. W.; Zhang, L.; Gong, C. H. Microwave absorption performance of reduced graphene oxide with negative imaginary permeability. *J. Phys. D: Appl. Phys*. **2020**, *53*, 02LT01.

[40] Wang, H. G.; Meng, F. B.; Huang, F.; Jing, C. F.; Li, Y.; Wei, W.; Zhou, Z. W. Interface modulating CNTs@PANi hybrids by controlled unzipping of the walls of CNTs to achieve tunable high-performance microwave absorption. *ACS Appl. Mater. Interfaces* **2019**, *11*, 12142–12153.

[41] Gu, J. W.; Lv, Z. Y.; Wu, Y. L.; Guo, Y. Q.; Tian, L. D.; Qiu, H.; Li, W. Z.; Zhang, Q. Y. Dielectric thermally conductive boron nitride/polyimide composites with outstanding thermal stabilities via *in-situ* polymerization-electrospinning-hot press method. *Compos. Part A: Appl. Sci. Manuf*. **2017**, *94*, 209–216.

[42] Wei, Y.; Zhang, L.; Gong, C. H.; Liu, S. C.; Zhang, M. M.; Shi, Y. P.; Zhang, J. W. Fabrication of TiN/carbon nanofibers by electrospinning and their electromagnetic wave absorption properties. *J. Alloys Compd*. **2018**, *735*, 1488–1493.

[43] Sun, X.; He, J. P.; Li, G. X.; Tang, J.; Wang, T.; Guo, Y. X.; Xue, H. R. Laminated magnetic graphene with enhanced electromagnetic wave

absorption properties. *J. Mater. Chem. C* **2013**, *1*, 765–777.
[44] Terao, T. Hopping electron model with geometrical frustration: Kinetic Monte Carlo simulations. *Eur. Phys. J. B* **2016**, *89*, 209.
[45] Gu, J. W.; Xu, S.; Zhuang, Q.; Tang, Y. S.; Kong, J. Hyperbranched polyborosilazane and boron nitride modified cyanate ester composite with low dielectric loss and desirable thermal conductivity. *IEEE Trans. Dielect. Electr. In.* **2017**, *24*, 784–790.
[46] Duan, Y. L.; Xiao, Z. H.; Yan, X. Y.; Gao, Z. F.; Tang, Y. S.; Hou, L. Q.; Li, Q.; Ning, G. Q.; Li, Y. F. Enhanced electromagnetic microwave absorption property of peapod-like MnO@carbon nanowires. *ACS Appl. Mater. Interfaces* **2018**, *10*, 40078–40087.
[47] Wang, Y.; Guan, H. T.; Du, S. F.; Wang, Y. D. A facile hydrothermal synthesis of MnO_2 nanorod–reduced graphene oxide nanocomposites possessing excellent microwave absorption properties. *RSC Adv.* **2015**, *5*, 88979–88988.
[48] Huang, L.; Li, J. J.; Li, Y. B.; He, X. D.; Yuan, Y. Fibrous composites with double-continuous conductive network for strong low-frequency microwave absorption. *Ind. Eng. Chem. Res.* **2019**, *58*, 11927–11938.
[49] Wang, Z. J.; Wu, L. N.; Zhou, J. G.; Cai, W.; Shen, B. Z.; Jiang, Z. H. Magnetite nanocrystals on multiwalled carbon nanotubes as a synergistic microwave absorber. *J. Phys. Chem. C* **2013**, *117*, 5446–5452.
[50] Zhang, X. F.; Guo, J. J.; Guan, P. F.; Qin, G. W.; Pennycook, S. J. Gigahertz dielectric polarization of substitutional single niobium atoms in defective graphitic layers. *Phys. Rev. Lett.* **2015**, *115*, 147601.
[51] Su, T. T.; Zhao, B.; Han, F. Q.; Fan, B. B.; Zhang, R. The effect of hydrothermal temperature on the crystallographic phase of MnO_2 and their microwave absorption properties. *J. Mater. Sci.: Mater. Electron.* **2019**, *30*, 475–484.
[52] Su, T. T.; Zhao, B.; Fan, B. B.; Li, H. X.; Zhang, R. Enhanced microwave absorption properties of novel hierarchical core-shell δ/α MnO_2 composites. *J. Solid State Chem.* **2019**, *273*, 192–198.
[53] Qiao, M. T.; Lei, X. F.; Ma, Y.; Tian, L. D.; Su, K. H.; Zhang, Q. Y. Dependency of tunable microwave absorption performance on morphology-controlled hierarchical shells for core-shell Fe_3O_4@MnO_2 composite microspheres. *Chem. Eng. J.* **2016**, *304*, 552–562.